SHRIMP U–Pb Zircon Ages, Geochemistry and Sr–Nd–Hf Isotope Systematics of the Zalute Intrusive Suite in the Southern Great Xing'an Range, NE China: Petrogenesis and Geodynamical Implications

Huanan Liu [1], Feng Yuan [2,*], Shengjin Zhao [1,3], Mingjing Fan [2,4] and Xiangguo Guo [1,5]

[1] State Key Laboratory of Geological Processes and Mineral Resources, School of Earth Sciences and Resources, China University of Geosciences, Beijing 100083, China; Huanan.Liu@cugb.edu.cn (H.L.); 3001140042@cugb.edu.cn (S.Z.); guoxiang_guo@126.com (X.G.)

[2] State Key Laboratory of Geological Processes and Mineral Resources, Collaborative Innovation Centre for Exploration of Strategic Mineral Resources, School of Earth Resources, China University of Geosciences, Wuhan 430074, China; fmingjing@cug.edu.cn

[3] No.10 Institute of Geological Exploration, Inner Mongolia Bureau of Geology and Mineral Resources, Chifeng 024005, China

[4] MNR Key Laboratory of Metallogeny and Mineral Assessment, Institute of Mineral Resources, Chinese Academy of Geological Sciences, Beijing 100037, China

[5] College of Mining Technology, Inner Mongolia University of Technology, Hohhot 010051, China

** Correspondence: yuanfengyf666@126.com; Tel.: +86-027-6788-2364

Abstract: An integrated zircon geochronological, elemental geochemical, and Sr–Nd–Hf isotopic investigation was carried out on a suite of dioritic–granitic rocks at Zalute in the southern Great Xing'an Range (SGXR), NE China, in order to probe the source and petrogenesis of these granitoid rocks and further constrain the geodynamical setting of early Early Cretaceous magmatism. The results of Sensitive High-Resolution Ion Micro Probe (SHRIMP) zircon U–Pb dating reveal that the Zalute dioritic–granitic rocks have a consistent crystallization age of ca. 137–136 Ma, consisting of quartz diorite (136 ± 1.4 Ma), monzogranite (136 ± 0.8 Ma), and granite porphyry (137 ± 1.3 Ma), which record an early Early Cretaceous magmatic intrusion. Geochemically, the quartz diorites, monzogranites, and granite porphyries are mostly high-K calc-alkaline and show features of typical I-type affinity. They possess uniform and depleted Sr–Nd–Hf isotopic compositions (e.g., initial $^{87}Sr/^{86}Sr$ ratios of 0.7035 to 0.7049, $\varepsilon_{Nd}(t)$ of −0.02 to +2.61, and $\varepsilon_{Hf}(t)$ of +6.8 to +9.6), reflecting a common source, whose parental magma is best explained as resulting from the partial melting of juvenile source rocks in the lower crust produced by underplating of mantle-derived mafic magma, with minor involvement of ancient crustal components. Evidence from their close spatio–temporal relationship, common source, and the compositional trend is consistent with a magmatic differentiation model of the intermediate-felsic intrusive suite, with continued fractional crystallization from quartz diorites, towards monzogranites, then to granite porphyries. Combined with previously published data in the SGXR, our new results indicate that the Zalute intermediate-felsic intrusive suite was formed during the post-collisional extension related to the closure of the Mongol–Okhotsk Ocean and subsequent slab break-off.

Keywords: SHRIMP U–Pb zircon ages; Sr–Nd–Hf isotope; early Early Cretaceous magmatism; petrogenesis; tectonic setting; southern Great Xing'an Range

1. Introduction

Granitoid rocks are widely considered to be one of the most important components of the continental crust, which are mainly generated by a massive transfer of heat and/or mantle materials to the crust in the various geodynamical settings [1–5]. An understanding of petrogenesis and geodynamical setting of granitoids are important for the interpretation of the crustal evolution and crust–mantle interaction [6–12].

The southern Great Xing'an Range (SGXR), situated in the southeastern Central Asian Orogenic Belt, is well-known for Late Mesozoic granitoid rocks [4,5,13]. There have been important advances in the research of Late Mesozoic granitoid magmatism in recent years. It is widely accepted that these granitoids were mainly formed in the Early Cretaceous, with subordinates in the Late Jurassic [14–16], which were mainly derived from partial melting of juvenile materials with near-zero to positive Hf–Nd isotopic characteristics [17–19] and mantle-like $\delta^{18}O$ compositions [16]. The large-scale Early Cretaceous granitoid magmatism is thought to be linked with the intracontinental extension [9,14]. Nevertheless, the magma genesis and geodynamic process of the Early Cretaceous giant granitoid-forming event are still not fully understood.

Several models have been proposed to decipher the origin and geodynamics of the Early Cretaceous granitoids in the SGXR, including (1) the "extreme fractional crystallization model of mantle-derived magma" which emphasizes evolved mantle-derived basaltic magma associated with the continental rifting [4]; (2) the "slab window model" advocates partial melting of subducting oceanic crust near the Mongol–Okhotsk ridge, accompanied with extension in the overlying lithosphere [20]; (3) the "mixing model" stresses on crust–mantle magma mixing, which is related to a post-collisional extensional setting [13,21,22]; (4) the "delamination model" proposes the gravitational collapse of thickened continental crust related to closure of the Mongol–Okhotsk Ocean [5,11,23,24] or subduction of the Paleo-Pacific Plate [25,26]; and (5) the "underplating model" argues for partial melting of underplated lower crust related to closure of the Mongol–Okhotsk Ocean [5,16] or superimposed by a far-field effect of western subduction of the Paleo-Pacific plate [14,15].

When compared to the northern part of the Great Xing'an Range, relatively few comprehensive studies have concentrated on the Early Cretaceous granitoids of the SGXR [13,27], which has hindered our understanding of Early Cretaceous tectonic-magmatism evolution in the SGXR [1].

In this work, we report new Sensitive High-Resolution Ion Micro Probe (SHRIMP) U–Pb zircon ages, major and trace elements, zircon Hf isotopic and whole-rock Sr–Nd isotopic data for quartz diorite, monzogranite, and granite porphyry at Zalute in the SGXR. The purpose of this study is to (1) constrain the magma source; (2) shed light on the petrogenesis of the dioritic–granitic rocks; and (3) provide insights into the tectonic setting that controlled the formation of the Early Cretaceous intermediate-felsic intrusive suite at Zalute.

2. Regional Geology

The Great Xing'an Range (GXR), located in the eastern part of Central Asian Orogenic Belt (Figure 1a), is sandwiched between the Siberia Craton to the north and North China Craton to the south [4,28–34]. It experienced a remarkable geological amalgamation as a result of continental collision events during the Phanerozoic [34], which were related to the subduction of the Paleo-Asian Ocean, Mongol–Okhotsk Ocean, and Paleo-Pacific Ocean during Paleozoic [35,36]. The Mongol–Okhotsk Suture to the northwest of the GXR (Figure 1b) is widely accepted as representing the final closure of the Paleo-Asian Ocean [15,37–39]. The subduction of the Paleo-Pacific oceanic plate is suggested to start in the Early Jurassic [40].

The SGXR lies at the southern segment of the GXR, bound to the north by the Erlian–Hegenshan fault, to the south by the Xar Moron fault, and to the northeast by the Nenjiang fault (Figure 1c) [36,41,42]. The Xilinhot Complex is mainly composed of Paleozoic mica schist, paragneiss, and biotite-bearing granitic gneiss, representing the oldest strata exposed in the SGXR [43]. Late Paleozoic to Mesozoic magmatic rocks widely intruded into the Permian metamorphic volcano-sedimentary associations,

limestones, and clastic rocks [44]. Late Mesozoic volcanic rocks in the SGXR have a wide range in the composition, which are dominantly composed of basaltic to rhyolitic rocks [20,35,44].

Late Paleozoic and Mesozoic intrusions consist mainly of quartz diorite, granodiorite, monzogranite, syenogranite, granite porphyry, quartz porphyry, and alkali granite, which are associated with the subduction and the closure of the Paleo-Asian and Mongol–Okhotsk oceanic slabs, subduction of the Paleo-Pacific oceanic slab, and subsequent lithospheric extension [14,45]. Among them, the large-scale Early Cretaceous granitoid magmatism occurs far from plate boundaries, which were associated with continental convergence and intracontinental orogenesis in East Asia [14,16,46]. Pre-Mesozoic faults are thought to be the major structure in the SGXR. The spatial distribution of the Early Cretaceous granitoid rocks is mainly controlled by NE-, NW-, and near E–W-striking normal faults (Figure 1c) [14].
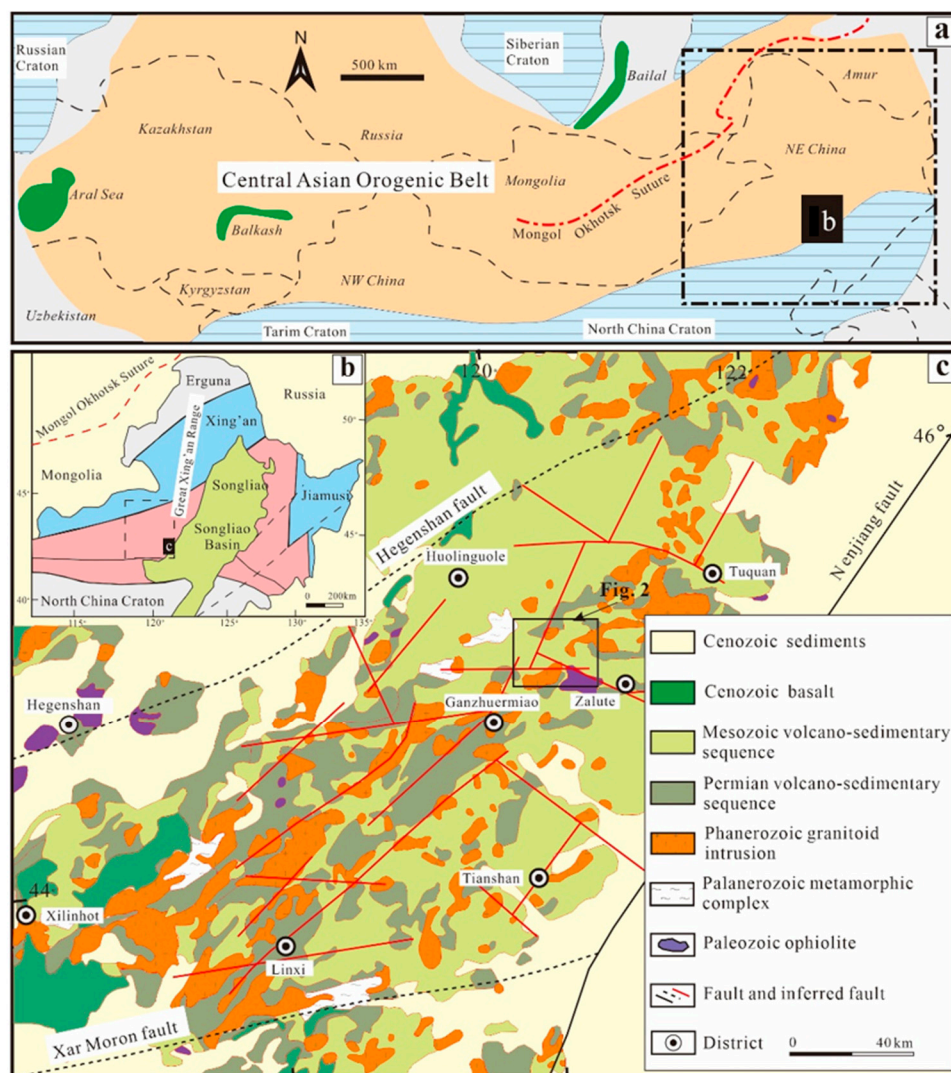

Figure 1. (**a**) Schematic map of the Central Asian Orogenic Belt (after Shen et al. [28]) showing the location of NE China; (**b**) Simplified geotectonic division of NE China (after Zhang et al. [37]), showing the location of the SGXR; and (**c**) Geologic sketch map of the southern Great Xing'an Range (SGXR) (modified after Ouyang et al. [14] and Guo et al. [41]).

The Zalute area is situated in the east part of the SGXR (Figure 1c). The lower Permian strata in the region is a volcanic rocks suite of neritic facies, interlayered with clastic rocks, mainly including meta-andesite, meta-dacitic tuff, and meta-sandstone. The Upper Permian strata are dominated

by a suite of clastic rocks of lacustrine facies, consisting of meta-siltstone, mudstone, felsic slate, and marlstone [27]. The Jurassic strata are mainly felsic volcanic rocks and clastic rocks of lacustrine facies, comprising andesite, volcanic breccia, volcanic tuff, conglomerate, sandstone, and shale. The Cretaceous strata consist of andesitic breccia, pyroclastic rock, tuff, limestone, and sandstone. The volcanic rocks exposed in this region involve the Late Jurassic Manketou'ebo Formation, and the Early Cretaceous Baiyingaolao, Manitu, and Meiletu Formations (Figure 2) [24]. The Late Jurassic Manketou'ebo Formation is characterized by rhyolite and tuff, whereas the Early Cretaceous Baiyingaolao, Manitu, and Meiletu Formations are comprised of andesite, basaltic andesite, dacite, rhyolite, tuff, and pyroclastic rock [24,44,47]. The Ealy Permian, Early Triassic, Late Jurassic, and Early Cretaceous intrusive rocks exposed in this region (Figure 2) are mainly composed of quartz diorite, quartz monzonite, monzogranite, granite porphyry, alkaline granite, and albite granite. These Early Permian to Early Cretaceous granitoid rocks commonly intruded in the form of batholiths, stocks, and dikes [18]. Major faults in the region are dominated by NW- and NE-striking faults, with subordinate E–W-striking faults.
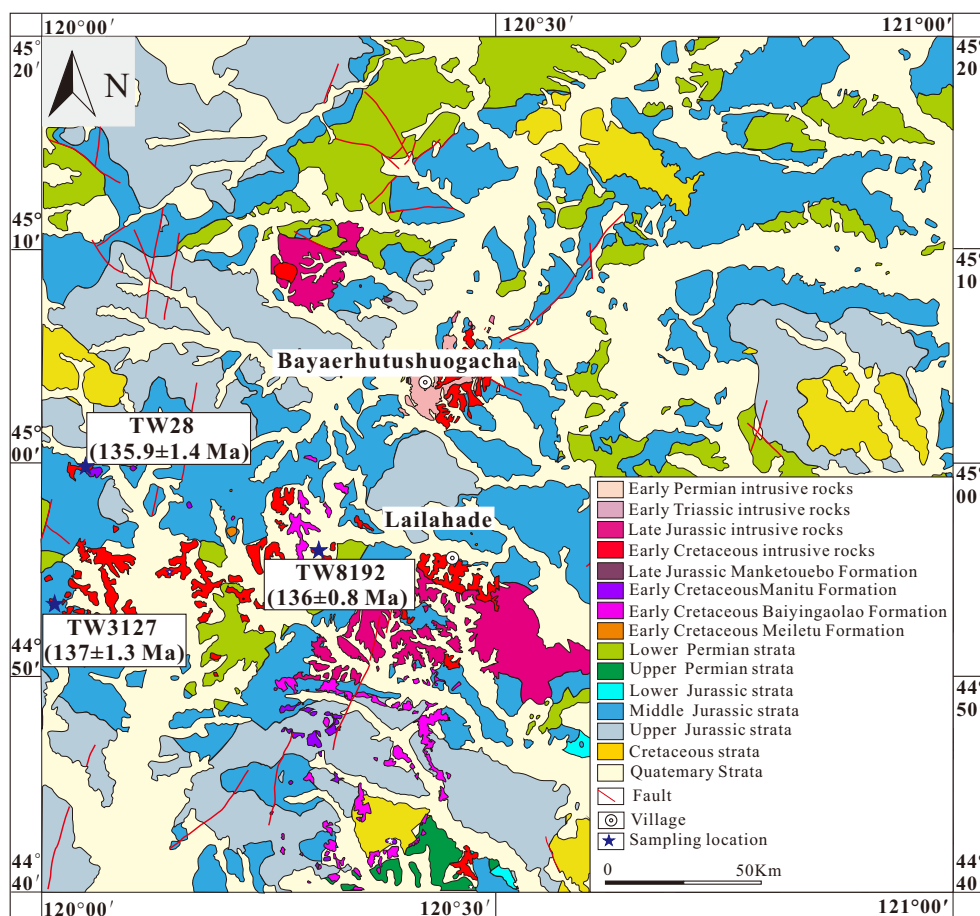

Figure 2. Simplified geological map of the Zalute area in the SGXR.

3. Sampling and Analytical Methods

3.1. Sample Descriptions

The granitoid samples collected from Zalute area include quartz diorite (Figure 3a,b), monzogranite (Figure 3c,d), and granite porphyry (Figure 3e,f). Sample locations are shown in Figure 2 and given in Supplementary Table S1.

Quartz diorites are characterized by a fine-grained, holocrystalline texture (Figure 3a), which mainly consists of plagioclase, quartz, biotite, and amphibole (Figure 3b) with accessory zircon, apatite, and titanite. Occasionally, amphibole and biotite grains occur as inclusions in plagioclase.

Plagioclase grains exhibit euhedral to subhedral with sizes spanning from 0.2 to 1.0 mm. Quartz grains mainly show anhedral with sizes varying from 0.1 to 0.4 mm. Biotite grains occur as euhedral crystals up to 0.8 mm long. Amphibole grains are euhedral to subhedral with sizes in the range of 0.1 to 0.3 mm.
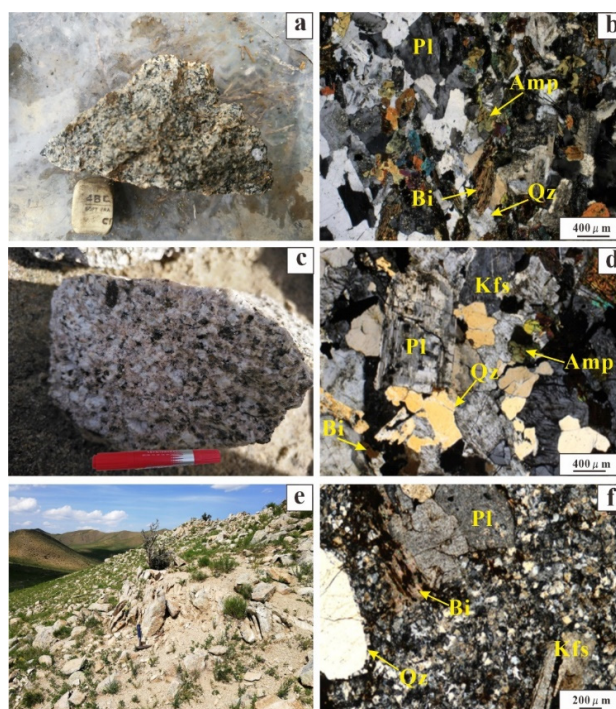

Figure 3. Photographs (left) and corresponding thin section photomicrographs (right) of the granitoids from Zalute. (**a**,**b**) Quartz diorite, (**c**,**d**) monzogranite, and (**e**,**f**) granite porphyry. Mineral abbreviations: Amp—amphibole; Bi—biotite; Pl—plagioclase; Kfs: K-feldspar; Qz—quartz.

Monzogranites show fine-to-medium-grained texture (Figure 3c). They mainly consist of plagioclase, K-feldspar, quartz, biotite, and amphibole (Figure 3d). Accessory minerals include apatite, zircon, monazite, and ilmenite. Plagioclase commonly occurs as euhedral grains up to 2 mm long. Occasionally, K-feldspar (up to 0.8 mm) contains small quartz inclusions. Quartz (0.1–0.8 mm) generally display subhedral grains. Biotite and amphibole grains are mainly euhedral to subhedral, occurring between the intervals or enclosed by quartz.

Granite porphyries are typically porphyritic with phenocrysts (up to 2 mm) of plagioclase, quartz, K-feldspar, and biotite (Figure 3e,f). Plagioclase and biotite phenocrysts are mainly euhedral or subhedral. K-feldspar phenocrysts occur as subhedral grains. Quartz phenocrysts occur as subhedral to anhedral grains in shape with rounded edges.

3.2. SHRIMP U–Pb Zircon Dating

Zircon grains were separated using conventional heavy liquids, hand-picking, and then mounted on epoxy resin and polished to expose the crystal interiors. To characterize internal structures of zircon grains and select better target sites for U–Pb dating, cathodoluminescence (CL) imaging was performed using a JXA-8800R Electron Probe at the Institute of Geology, Chinese Academy of Geological Sciences (CAGS), Beijing, China. Zircon U–Pb isotopic analyses of all the samples were carried out using a Sensitive High-Resolution Ion Micro Probe (SHRIMP) II following the method of Williams [48], at the Beijing SHRIMP Center, CAGS, Beijing, China. International standard SL13 (572 Ma) and TEMORA (417 Ma) were used for the test procedure as discussed by Black et al. [49]. For the sake of monitoring the contents of U, Th, and Pb, one SL13 reference sample was run for every nine analyses of the samples with a beam diameter of 30–40 μm. To maintain the precision of the measured results, one TEMORA reference sample was run for every four analyses of the samples.

Detailed analytical procedures followed those described by Song [50]. The weighted mean ages were calculated, and Concordia diagrams were conducted using Isoplot (Ex ver3, Berkeley Geochronology Center, Berkeley, CA, USA) [51].

3.3. Zircon Hf Isotopes

In situ Lu–Hf isotopic analyses were conducted by using a Neptune Plus multi-collector inductively coupled plasma mass spectrometry (MC–ICP–MS) (Thermo Fisher Scientific, Erlangen, Germany), attached to a GeoLas HD excimer ArF laser ablation (LA) system (Coherent, Göttingen, Germany) that is hosted at the Wuhan Sample Solution Analytical Technology Co., Ltd., Hubei. To correlate LA–MC–ICP–MS zircon Hf isotope data with U–Pb isotope data, analytical spots were situated close to or overlapping with the SHRIMP measure spots. A spot size of the laser was set to 44 μm, with a laser repetition rate of 8 Hz and an energy density of ~7.0 J/cm^2. To track the accuracy of analysis, zircon standards 91,500 and GJ-1 were used as reference samples, yielding weighted mean ^{176}Hf/^{177}Hf ratios of 0.282295 ± 0.000005 (2σ) and 0.282000 ± 0.000009 (2σ), respectively, which are good agreement with their recommended ratios. Detailed operating conditions can be found in Hu et al. [52]. Off-line selection, integration of analyte signals, and mass bias calibrations were made using soft ICPMSDataCal10.7 [53].

3.4. Major and Trace Elements

The samples were first powdered to ~200 mesh. Then, major and trace element analyses of whole-rock were conducted at Createch Testing Technology Co., Ltd., Beijing. China. Major element analyses were performed by X-ray fluorescence spectrometry (XRF-1800). The analytical error and accuracy for major elements are generally better than 1% based on analyses of national rock standards (GSR-1, GSR-2, GSR-3, GSD-9, BHVO-2, and AGV-2). Trace element analyses of whole-rock were analyzed using Agilent 7500ce inductively coupled plasma mass spectrometry (ICP–MS). The detailed analytical procedures followed those described by Wei et al. [54].

3.5. Sr and Nd Isotopes

The Sr and Nd isotopic compositions were determined by using a multi-collector (MC) –ICP–MS (Neptune Plus, Thermo-Fisher) at Createch Test Technology Co. Ltd., Beijing, China. Detailed analytical procedures can be found in Yang et al. [55]. The ratios of ^{87}Rb/^{86}Sr and ^{147}Sm/^{144}Nd were calculated from Rb, Sr, Sm, and Nd concentrations measured by ICP–MS. During the analytical process, the average ^{147}Sm/^{144}Nd ratios for international basalt standard BHVO-2 and BCR-2 were 0.1542 (2σ, *n* = 17) and 0.1405 (2σ, *n* = 17), respectively. The average ^{143}Nd/^{144}Nd ratios for standard BHVO-2 and BCR-2 were 0.512964 ± 5 (2σ, *n* = 17) and 0.512608 ± 5 (2σ, *n* = 17), respectively, which are within the error of those reported by Li et al. [56]. The Sr isotope international standard NBS 987 was repeatedly tested for monitoring the accuracy of the test results, yielding an average ^{87}Sr/^{86}Sr ratio of 0.710247 ± 13 (2σ, *n* = 17), which is close to that reported by Zhai et al. [57].

4. Analytical Results

4.1. Zircon U–Pb Age Data

The zircon SHRIMP U–Pb age data are listed in Supplementary Table S1. Zircon grains from the quartz diorite (sample TW28) show euhedral to subhedral, prismatic, and transparent, spanning from 60 to 140 μm in length. Their weakly oscillatory zoning is visible in CL images (Figure 4a). Fifteen spots from fifteen zircon grains were carried out for U–Pb dating. These zircon grains have 824–891 ppm U and 178–912 ppm Th, with Th/U ratios in the range of 0.6–1.0, indicating a magmatic origin. The results gave ^{206}Pb/^{238}U ages ranging from 134 to 139 Ma. These analyses fall closely on the Concordia, yielding a weighted mean ^{206}Pb/^{238}U age of 136 ± 1.4 Ma (MSWD = 0.25; Figure 4a), which represents the crystallization age of quartz diorite.

Zircon grains from the monzogranite (sample TW8192) are euhedral to subhedral, varying from 70 to 160 μm in length. They are transparent and prismatic, with well-developed oscillatory zoning visible in CL images (Figure 4b). The zircon grains possess 506–1407 ppm U and 198–1065 ppm Th, with Th/U ratios in the range of 0.33 to 0.76, suggesting a magmatic origin. Sixteen spots were performed on sixteen zircon grains for U–Pb dating, yielding $^{206}Pb/^{238}U$ ages spanning from 133 to 139 Ma. The concordant to sub-concordant analyses yield a weighted mean $^{206}Pb/^{238}U$ age of 136 ± 0.8 Ma (MSWD = 0.91; Figure 4b), which is interpreted as the crystallization age of monzogranite.
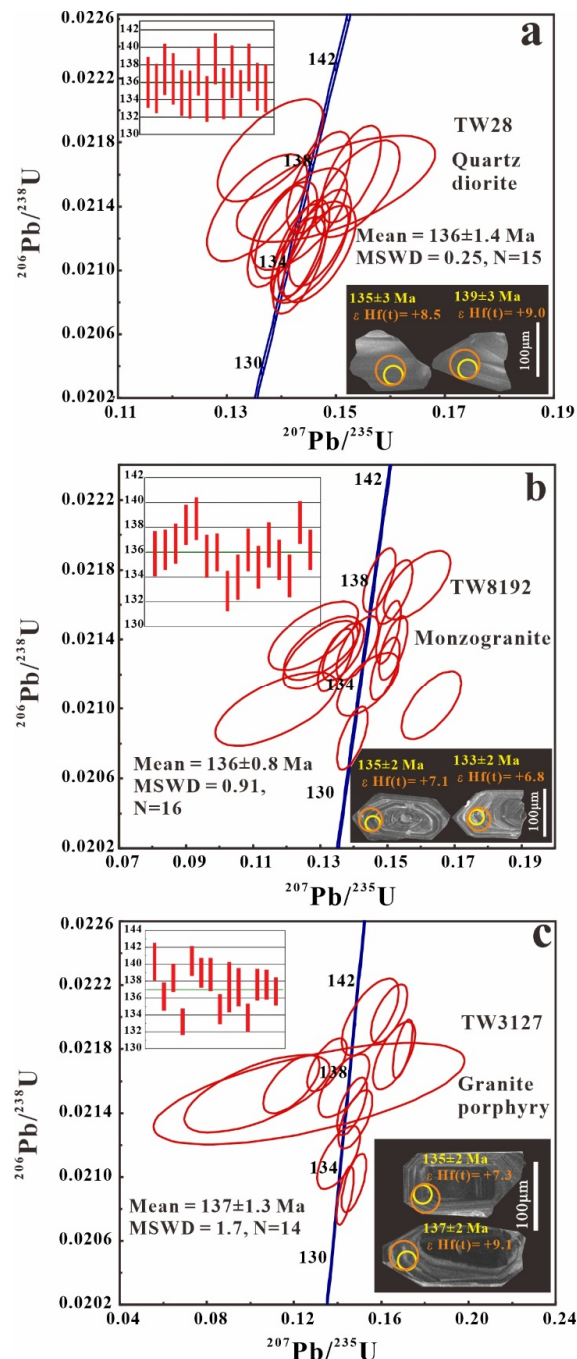

Figure 4. Representative cathodoluminescence (CL) images and U–Pb Concordia diagrams of zircon from the Zalute granitoids. The insets show their corresponding weighted diagrams in the Zhalute area. (**a**) Quartz diorite, (**b**) monzogranite, and (**c**) the granite porphyry. The yellow circles show zircon U–Pb dating spots and corresponding U–Pb ages (Ma), and the orange circles show Lu–Hf isotope analysis spots and corresponding $\varepsilon_{Hf}(t)$ values.

Zircon grains from the granite porphyry (sample TW3127) are transparent, prismatic, and euhedral, and are 80–200 μm in length. CL images reveal that they have apparent concentric zoning (Figure 4c). Fourteen spots were performed on fourteen zircon grains for U–Pb dating. These zircon grains have 227–1937 ppm U and 158–1412 ppm Th, with Th/U ratios of 0.4–1.18, indicating a magmatic origin. The results gave $^{206}Pb/^{238}U$ ages varying from 129 to 140 Ma. The concordant to sub-concordant analyses yield a weighted mean $^{206}Pb/^{238}U$ age of 137 ± 1.3 Ma (MSWD = 1.7; Figure 4c), which represents the crystallization age of granite porphyry.

4.2. Zircon Hf Isotopic Data

The zircon Hf isotopic data are given in Supplementary Table S2 and shown in Figure 5a. Eight zircon grains from the quartz diorite (sample TW28) were measured for in situ Hf isotope analyses. Their $\varepsilon_{Hf}(t)$ are restricted to high values of +8.1 to +9.6, corresponding to crustal Hf model ages ($T_{DM}{}^C$) of 0.58 to 0.68 Ga.

Nine zircon grains from the monzogranite (sample TW8192) were determined for in situ Hf isotope analyses. The variation of $\varepsilon_{Hf}(t)$ is limited (+6.8 to +7.8), corresponding to $T_{DM}{}^C$ ages of 0.7 to 0.76 Ga.

Eight zircon grains from the granite porphyry (sample TW3127) were measured for in situ Hf isotope analyses. They also possess a restricted range of $\varepsilon_{Hf}(t)$ values from +7.4 to +9.1, corresponding to $T_{DM}{}^C$ ages of 0.61 to 0.73 Ga.

4.3. Major and Trace Element Data

The major and trace element data for the Zalute granitoids are present in Supplementary Table S3. As shown in the total alkalis–silica (TAS) (($K_2O + Na_2O$) versus SiO_2) diagram, the quartz diorite samples straddle the line between the diorite and monzonite field, and the monzogranite and granite porphyry samples plot mainly in the field of quartz-monzonite and granite, respectively (Figure 6a).
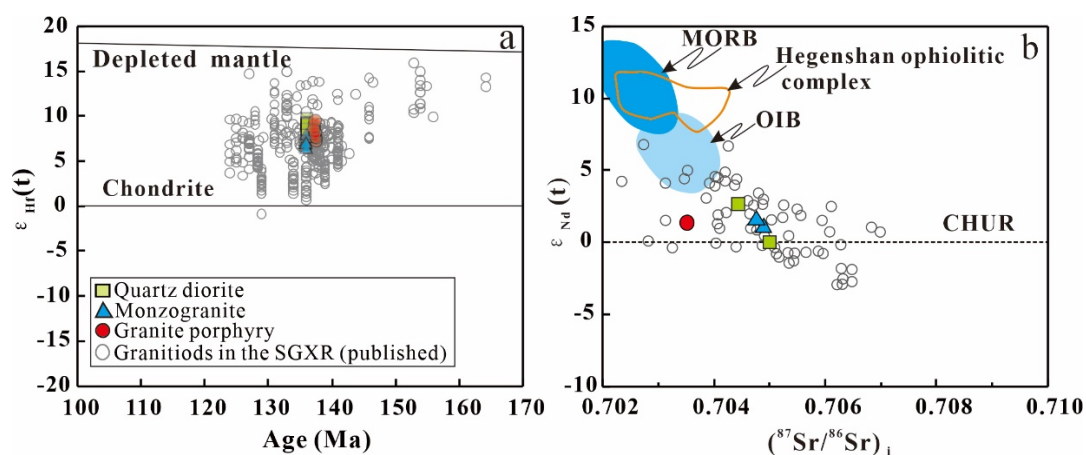

Figure 5. (**a**) Zircon U–Pb age versus $\varepsilon_{Hf}(t)$ diagrams for the granitoids from Zalute; (**b**) Sr–Nd isotope diagrams for the granitoids from Zalute. Data sources are from previously published Sr–Nd–Hf isotopic data for the SGXR [9,17,18,27,58–60].

The quartz diorite samples are characterized by moderate SiO_2 contents (60–62.6 wt.%) and relatively high contents of CaO (4.05–5.71 wt.%; Figure 7a), MgO (1.26–3.60 wt.%; Figure 7b), $Fe_2O_3{}^T$ (4.91–6.62 wt.%; Figure 7c), and TiO_2 (0.6–1.04 wt.%; Figure 7d), with a medium differentiation index (60–70). They exhibit variable P_2O_5 (0.02–0.20 wt.%; Figure 7e) and K_2O contents (1.5–2.8 wt.%; Figure 6b), most of which belong to high-K calc-alkaline series (Figure 6b). All samples possess a limited variety of Na_2O (3.92–4.95 wt.%; Figure 6c) and Al_2O_3 contents (17.4–18 wt.%; Figure 7f), with relatively variable A/CNK (molar $Al_2O_3/(CaO + Na_2O + K_2O)$) values varying from 0.83 to 1.04,

displaying metaluminous to weakly peraluminous characteristics (Figure 6d). Moreover, they show relatively high Sr (530–962 ppm; Figure 7g) and Ni contents (6.7–13.8 ppm; Figure 7h). The quartz diorite samples exhibit fractionated REE patterns (Figure 8a; La_N/Yb_N = 7–13), with negative to weakly positive Eu anomalies (Eu/Eu* = 0.56–1.09). In the primitive mantle-normalized trace element patterns (Figure 8b), they are enriched in large ion lithophile elements (LILE) (e.g., K, Pb, and Sr) and depleted in high field strength elements (HFSE) (e.g., Nb, Ta, and Ti).
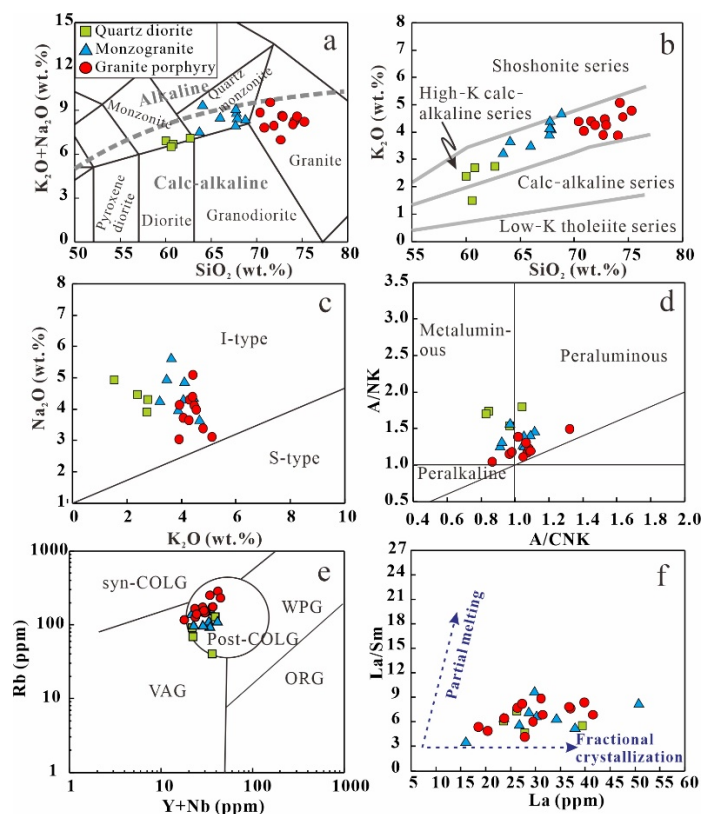

Figure 6. Selected discrimination diagrams for the granitoids from Zalute. (**a**) Total alkalis versus silica classification [61]; (**b**) SiO_2 versus K_2O [62]; (**c**) Na_2O versus K_2O [63]; (**d**) A/NK (molar $Al_2O_3/(Na_2O + K_2O)$) versus A/CNK (molar $Al_2O_3/(CaO + Na_2O + K_2O)$) [64]; (**e**) Rb versus (Y + Nb) [65]; and (**f**) La/Sm versus La diagrams [66]. WPG: within-plate granite; VAG: volcanic arc granite; Syn COLG: syn-collisional granite; Post-COLG: post-collisional granite; and ORG: ocean ridge granite.

By contrast, the monzogranite samples display elevated SiO_2 contents (63.4–68.8 wt.%) and lower contents of CaO (1.4–3.5 wt.%; Figure 7a), MgO (0.63–1.57 wt.%; Figure 7b), $Fe_2O_3{}^T$ (3.12–5.62 wt.%; Figure 7c), TiO_2 (0.41–0.8 wt.%; Figure 7d), P_2O_5 (0.04–0.19 wt.%; Figure 7e), Al_2O_3 (14.8–16.6 wt.%; Figure 7f), Sr (203–494 ppm; Figure 7g), and Ni (4.1–7.6 ppm; Figure 7h), with elevated differentiation index (73–86). These samples are metaluminous to weakly peraluminous (Figure 6d) with A/CNK values of 0.91–1.12 and are characterized by high K_2O (3.21–4.66 wt.%; Figure 6b) but variable Na_2O (3.62–5.62 wt.%) (Figure 6c), plotting in the high-K calc-alkaline field (Figure 6b). The chondrite-normalized REE diagram of the monzogranite samples (Figure 8a) shows fractionated REE patterns (La_N/Yb_N = 4–17), with negative Eu anomalies (Eu/Eu* = 0.46–0.95). Their primitive mantle-normalized trace element patterns (Figure 8b) are enriched in Rb, Th, K, and Pb relative to Ba, Nb, P, and Ti.

The granite porphyry samples, with high SiO_2 contents of 70.4 to 74.5 wt.% and high differentiation index (83–94), belong to the high-K calc-alkaline series with high K_2O contents (3.9–5.1 wt.%; Figure 6b). They are characterized by variable Na_2O (3.04–5.1 wt.%; Figure 6c) but low contents of CaO (0.43–2.12 wt.%; Figure 7a), MgO (0.31–1.04 wt.%; Figure 7b), $Fe_2O_3{}^T$ (1.88–3.03 wt.%; Figure 7c),

TiO_2 (0.17–0.35 wt.%; Figure 7d), P_2O_5 (0.01–0.13 wt.%; Figure 7e), Al_2O_3 (12.9–14.8 wt.%; Figure 7f), Sr (20–198 ppm; Figure 7g), and Ni (2.4–5.3 ppm; Figure 7h). These samples are metaluminous to peraluminous with variable A/CNK values of 0.86–1.32 (Figure 6d). They also display fractionated REE patterns (Figure 8a; La_N/Yb_N = 4–16), with medium to strongly negative Eu anomalies (Eu/Eu* = 0.08–0.65). As shown in the primitive mantle-normalized trace element patterns (Figure 8b), the granite porphyry samples are enriched in LILE (e.g., K and Pb) and depleted in HFSE (e.g., Nb, Ta, and Ti).
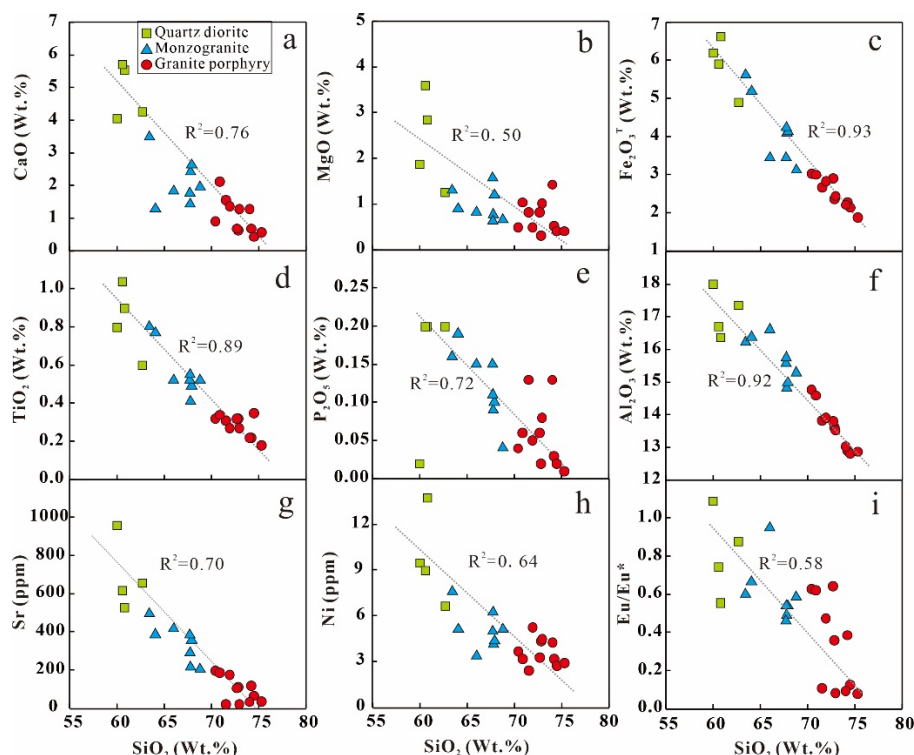

Figure 7. Harker diagrams for the granitoids from Zalute. SiO_2 versus CaO (**a**); MgO (**b**); $Fe_2O_3{}^T$ (**c**); TiO_2 (**d**); P_2O_5 (**e**); Al_2O_3 (**f**); Sr (**g**); Ni (**h**); and Eu/Eu* (**i**).
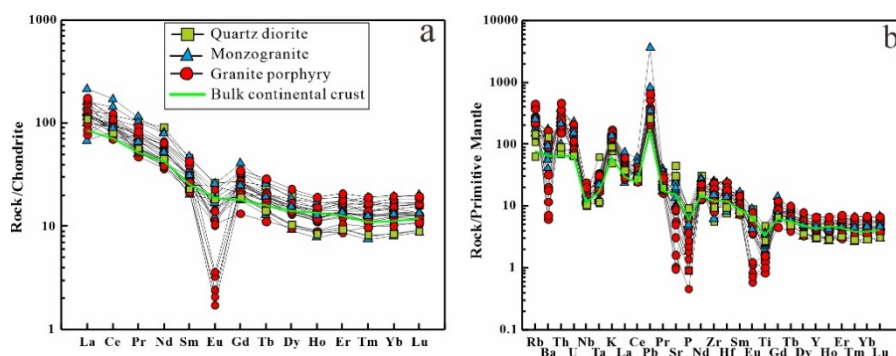

Figure 8. (**a**) Chondrite-normalized REE patterns and (**b**) primitive mantle normalized trace element patterns for the granitoids from Zalute. Chondrite and primitive mantle normalized values and composition of bulk continent crust can be found in Sun and McDonough [67].

4.4. Whole-Rock Sr–Nd Isotopic Data

Whole-rock Sr–Nd isotopic data for the Zalute granitoids are listed in Supplementary Table S4 and shown in Figure 5b. Initial Sr and Nd isotopic ratios were calculated at their zircon weighted mean $^{206}Pb/^{238}U$ ages. The quartz diorite samples exhibit high and uniform initial $^{87}Sr/^{86}Sr$ ratios of

0.7044–0.7049 and near-zero to positive $\varepsilon_{Nd}(t)$ values of −0.02 to +2.61, corresponding to two-stage Nd model ages (T_{DM2}) of 0.72 to 0.93 Ga. The monzogranite samples also show depleted Sr–Nd isotopic compositions, with initial $^{87}Sr/^{86}Sr$ ratios of 0.7048–0.7049 and $\varepsilon_{Nd}(t)$ values of +0.98 to +1.5, corresponding to T_{DM2} ages of 0.81 to 0.82 Ga. The granite porphyry sample has an initial $^{87}Sr/^{86}Sr$ ratio of 0.7035, $\varepsilon_{Nd}(t)$ value of +1.37, and T_{DM2} ages of 0.82 Ga, which are close to those of the quartz diorite and monzogranite samples.

5. Discussion

5.1. Timing of the Zalute Intrusive Suite

The intermediate-felsic intrusive suite (e.g., quartz diorite, quartz monzonite, monzogranite, and granite porphyry) and alkaline intrusive suite (e.g., alkaline granite and albite granite) are distributed at Zalute. Previous studies mainly focused on the geochronology of the alkaline intrusive suite associated with the Baerzhe rare metal deposit [68–71]. For example, alkaline granites were constrained at 127–121 Ma by Rb–Sr whole-rock isochron, LA–ICP–MS and SIMS zircon U–Pb dating, respectively [68–71]. Furthermore, Rb–Sr whole-rock isochron dating yielded an age of 125.2 ± 2 Ma for albite granite [70].

Although Shen et al. [72] reported a SHRIMP zircon U–Pb age of 137.4 ± 0.9 Ma for a quartz monzonite sample, few studies were undertaken for widespread quartz diorites, monzogranites, and granite porphyries at Zalute, which are the focus of this study. Here we present new ages of quartz diorite (136 ± 1.4 Ma), monzogranite (136 ± 0.8 Ma), and granite porphyry (137 ± 1.3 Ma) by SHRIMP zircon U–Pb dating (Figure 4). Based on the above chronological constraints, the intermediate-felsic intrusive rocks at Zalute show a consistent crystallization age of ~137–136 Ma, which is earlier than the alkaline intrusive rocks of ~127–121 Ma.

The Zalute intermediate-felsic intrusive suite is broadly coeval with or slightly earlier than the Early Cretaceous granitoids in the surrounding regions, such as diorites, monzogranites, and granite porphyries at Linxi (~135–125 Ma) [16,18,58], monzogranites at Ganzhuermiao (~139–125 Ma) [73], and monzogranites and syenogranites at Xilinhot–Huolinguole (~139–121 Ma) [60,74]. The widespread occurrences of these granitoids in the SGXR record an Early Cretaceous giant igneous event of the eastern Central Asian Orogenic Belt [5,16]. Integrating our new data with previous studies in the SGXR (Figure 5a), the early Early Cretaceous intermediate-felsic intrusive suite and middle Early Cretaceous alkaline intrusive suite can be distinguished, representing two magmatic pulses with an age gap of more than 10 Ma. Although many studies have been conducted on the late-stage alkaline granitoids associated with the Baerzhe rare metal deposit [68–71], little is known about the early-stage intermediate-felsic granitoids at Zalute. In what follows, we focus only on the early Early Cretaceous intermediate-felsic intrusive suite.

5.2. Magma Sources and Petrogenesis

5.2.1. Source Nature

The quartz diorite, monzogranite, and granite porphyry at Zalute have uniform and highly positive $\varepsilon_{Hf}(t)$ values (+8.1 to +9.6, +6.8 to +7.8, and +7.4 to +9.1, respectively; Figure 5a), near-zero to positive $\varepsilon_{Nd}(t)$ values (0.98 to 2.61) and low initial $^{87}Sr/^{86}Sr$ ratios (0.7035 to 0.7049; Figure 5b), suggesting that they share the similar parental magma derived from juvenile source rocks. Furthermore, the occurrence of negative $\varepsilon_{Nd}(t)$ value (−0.02) of one sample implies the involvement of minor ancient crustal materials during magma generation.

In general, the magma sources with juvenile isotopic signatures can be produced by (1) the evolved mantle-derived basaltic magma [75,76]; (2) underplated oceanic crust [2,77]; (3) magma mixing [4,13,21,22]; and (4) juvenile lower crust [5]. As outlined below, the first three possible source

candidates may be precluded for the origin of the studied granitoids. Instead, we consider that the best source candidate is juvenile lower crust.

1. The studied granitoids have high SiO_2 contents (up to 75.3 wt.%), implying that their parental magma may not derive directly from mantle-melting [47,78]. Moreover, the less evolved quartz diorites (SiO_2 contents of 60.0 to 62.6 wt.%) have relatively low MgO (1.26 to 3.6 wt.%, average 2.39 wt.%; Figure 7b), Cr (4 to 38 ppm, average 21 ppm), and Ni contents (7 to 14 ppm, average 10 ppm; Figure 7h). This argues against the case of mantle-derived melts, which are characterized by high MgO (>5% wt.%) (e.g., melts from the metasomatized mantle wedge) [79], Cr (~200 ppm), and Ni contents (~100 ppm) (e.g., high-Mg diorites) [80,81]. Furthermore, fractional crystallization of mantle-derived basaltic magma is commonly accompanied by mafic or ultramafic cumulates [75], which were not found at Zalute [72]. Accordingly, the extreme differentiation model of mantle-derived magma may be precluded.

2. Niu et al. [2] and Xiao et al. [82] argued that the juvenile isotopic signatures of granitoids can be inherited from the underplated oceanic crust. The resultant granitoids generally mixed with a large amount of ancient crustal materials in the sources, leading to large variation in $\varepsilon_{Hf}(t)$ and enrichment $\varepsilon_{Nd}(t)$ values, as exemplified by the granitoids from the West Kunlun Orogen [83], North Qilian Orogen [84,85], and West Qinling Orogen [86]. However, this is not in agreement with the case of the Zalute granitoids, which are characterized by uniform and high positive $\varepsilon_{Hf}(t)$ (Figure 5a) and depleted $\varepsilon_{Nd}(t)$ values (Figure 5b). Furthermore, the granitoids derived from the underplated oceanic crust are expected to be formed in a syn-collision setting [2,77]. Nevertheless, a plot of Y + Nb versus Rb (Figure 6e) reveals that the Zalute intermediate-felsic granitoid samples are mainly plotted in the post-collisional granite field, indicating an extension setting. In addition, it is widely accepted that the SGXR has experienced lithospheric extension since the early Early Cretaceous [21,27,87]. Thus, the Zalute granitoids are difficult to explain with the underplated oceanic crust model.

3. The granitoids formed by magma mixing commonly show resorption texture or reversed zoning in plagioclase [84], which is not consistent with what we observed in the studied granitoids (Figure 3). Moreover, the lack of mafic microgranular enclaves in the granitoids at Zalute also excluded the magma mixing model [14,22]. Moreover, the granitoids formed by magma mixing are expected to have a wide range of $\varepsilon_{Hf}(t)$ values (generally more than 10 units) due to incomplete mixing [88], which conflict with the uniform $\varepsilon_{Hf}(t)$ values (+6.8 to +9.6) of the studied samples (Figure 5a). Therefore, the magma mixing model is insufficient to explain the source of the Zalute granitoids.

4. The Zalute granitoids are characterized by "crustal-like" geochemical features, such as enrichment in the LREE and LILE, and depletion in the HFSE (Nb, Ta and Ti) (Figure 8), implying that their parental magmas are likely to be produced from the continental crust [47]. Moreover, the granitoids show relatively low Ce/Pb (mainly 0.4 to 5.2; average 2.6) and Nb/Ta ratios (3.9 to 15.6; average 11.9). Their Ce/Pb and Nb/Ta ratios are evidently lower than those of primitive mantle (Ce/Pb = 9 and Nb/Ta = 17.5) but close to continental crust (Ce/Pb = 4 and Nb/Ta = 11–12) [89,90], further implying a crustal origin [32]. Accordingly, we propose that the Zalute intermediate-felsic intrusive suite was mainly derived from juvenile source rocks in the lower crust (cf. [1,9,17,18]).

5.2.2. Granite Type and Fractional Crystallization

In terms of source nature and geochemical characteristics, granitoids have been generally classified as I-, S-, and A-types [78,91,92]. The early Early Cretaceous granitoids at Zalute have relatively low zircon saturation temperatures (665 °C–816 °C; average 753 °C) according to the zircon saturation thermometer of Boehnke et al. [93], similar to those of typical I-type granite (~760 °C) but significantly lower than those of typical A-type granite (~840 °C) [94]. Most samples (exceptionally samples D9723 and D4449) are metaluminous to weakly peraluminous (Figure 6d), which are different from strongly peraluminous S-type granites [95]. Furthermore, the absence of aluminous minerals such as garnet, muscovite, and tourmaline further rules out their affinity with S-type granites. Only two samples

display strongly peraluminous features with high A/CNK values of 1.12 and 1.32, which may be caused by magmatic fractionation [78,96].

The metaluminous to weakly peraluminous melts forming I-type granites are characterized by the low solubility of P and its decrease as the melt evolves, resulting in P_2O_5 decreasing with increasing SiO_2 in the I-type melts [97]. By contrast, the strongly peraluminous melts forming S-type granites are unsaturated in P, hence no definite trend of decreasing P_2O_5 with the increase in SiO_2 in the S-type melts [57,98]. Therefore, the contrasting behaviors of P between I- and S-type melts can be used to effectively distinguish between them [78]. Plotting P_2O_5 against SiO_2 for the Zalute granitoids reveals a strongly negative correlation between them (Figure 7e), indicating a chemical affinity to I-type granite. This observation can be further reinforced by the K_2O versus Na_2O discrimination diagram that all the samples were plotted in the field of I-type granite (Figure 6c) [63]. Accordingly, the intermediate-felsic intrusive suite at Zalute is I-type granites.

Combination of geochronological, Sr–Nd–Hf isotopic, and whole-rock chemical data support a magmatic differentiation model of an intermediate-felsic granitic system, with a close petrogenetic relationship between quartz diorite, monzogranite, and granite porphyry at Zalute, as indicated by the following lines of evidence.

1. The quartz diorites, monzogranites, and granite porphyries (~137–136 Ma; Figure 4) have a close spatial–temporal relationship.

2. In plots of $\varepsilon_{Hf}(t)$ value versus age (Figure 5a) and initial $^{87}Sr/^{86}Sr$ ratio versus $\varepsilon_{Nd}(t)$ value (Figure 5b), these granitoid samples are indistinguishable or overlapping within a narrow range in terms of their Sr–Nd–Hf isotopic compositions, indicating a common source.

3. The quartz diorites, monzogranites, and granite porphyries display similar chondrite-normalized REE patterns (Figure 8a) and primitive mantle-normalized trace element patterns (Figure 8b). Moreover, these granitoids show clear trends in chemical compositions defining linear regressions on variation diagrams, where the selected elements correlate negatively with SiO_2 (Figure 7), resulting from either partial melting or fractional crystallization. It is widely assumed that the effects of these two processes can be evaluated and distinguished by a La/Sm versus La diagram [29,66]. As shown in Figure 6f, the fractional crystallization process played a more important role in the evolution of the Zalute intermediate-felsic granitoid magmatism. This observation is further supported by the differentiation index increasing gradually from quartz diorites (60–70), toward monzogranites (73–86), then to granite porphyries (83–94).

4. Fractional crystallization has taken place in the intermediate-felsic magmatic system, as indicated by the pronounced depletion in Nb, Ti, and Eu (Figure 8a,b). The marked negative anomalies of Nb and Ti are thought to be related to the fractionation of biotite [99]. Previous studies have demonstrated that biotite/melt partition coefficients are significantly higher for V and Sc relative to Th, resulting in Th partitioned more strongly into the residual melts than V and Sc during biotite crystallization, and hence lower V/Th and Sc/Th ratios, accompanied with increasing SiO_2/Al_2O_3 ratios in the residual melts [100,101]. Our granitoid samples exhibit negative correlations with SiO_2/Al_2O_3 by V/Th (Figure 9a) and Sc/Th (Figure 9b), as well as SiO_2 by Al_2O_3 (Figure 7f) and TiO_2 (Figure 7d), indicating biotite fractionation. Negative correlations with SiO_2 are also shown by CaO (Figure 7a), and Sr (Figure 7g), and Eu/Eu* (Figure 7i), implying fractionation of plagioclase and/or K-feldspar. The MgO (Figure 7b), $Fe_2O_3^T$ (Figure 7c), and Ni (Figure 7h) of the granitoids are negatively correlated with SiO_2, which are related to the fractionation of amphibole [102]. A negative correlation between P_2O_5 and SiO_2 (Figure 7e) resulted from apatite fractionation [103].

Taking all the above considerations into account, the parental melts equivalent to the early Early Cretaceous granitoids at Zalute were generated by partial melting of juvenile source rocks in the lower crust induced by mantle-derived magmatic underplating, followed by continued fractional crystallization from quartz diorites, towards monzogranites, then to granite porphyries.
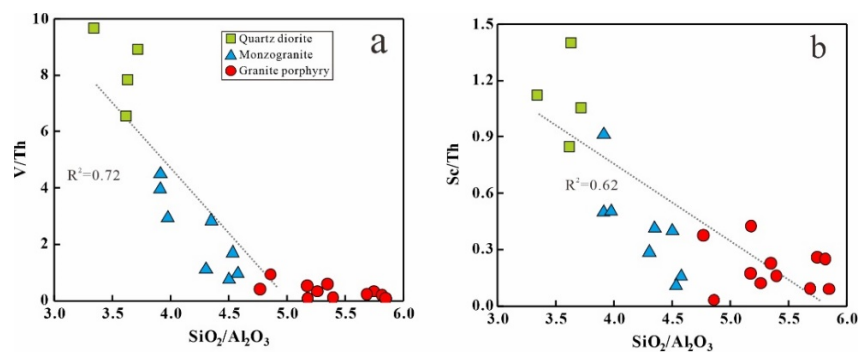
Figure 9. SiO_2/Al_2O_3 versus V/Th (**a**) and Sc/Th (**b**) for the granitoids from Zalute.

5.3. Geodynamic Implications

The geodynamic setting of the Early Cretaceous magmatic rocks in the SGXR has been hotly debated over the past several decades. Five scenarios have been proposed as follows: (1) mantle plume-rift-extension or other intraplate processes [35,76,104]; (2) lithospheric extension related to ridge subduction of the Mongol–Okhotsk Ocean and a resultant slab window [20]; (3) delamination of thickened crust related to the closure of the Mongol–Okhotsk Ocean [5,11,23,24] or subduction and subsequent retreat of the Paleo-Pacific oceanic slab [25,26,45,105]; (4) combination effects of lithospheric extension associated with break-off of the Mongol–Okhotsk oceanic slab and rollback of the Paleo-Pacific oceanic slab generating back-arc spreading [14,15]; and (5) post-collisional extension related to the scissor-type closure of the Mongol–Okhotsk Ocean [5,11,16,106,107].

Based on Early Cretaceous basaltic rocks characterized by both intraplate and volcanic arc geochemical properties, Ge et al. [76] proposed that the mantle plume hypothesis could interpret the Early Cretaceous magmatism in the SGXR. Larson and Olson [108] suggested that the process of rifting above a mantle plume commonly produces a circular- or ring-shape distribution pattern of magmatic rocks, which conflicts with the Early Cretaceous NE-trending granitoid belt in the SGXR [9,16]. Furthermore, such Early Cretaceous granitoid magmatism lasted for at least ~25 Ma, which also argues against the mantle plume model that related magmatism is thought to continue for only a few million years due to the rapid upwelling mantle plume [44].

Widespread adakitic rocks, high-Mg andesites, and tholeiite are typical products of the slab window-related subduction [20,58,109]. However, these magmatic rocks were not found at Zalute, precluding the possibility of a slab window model in the generation of the studied intermediate-felsic intrusive suite.

The Early Cretaceous granitoids occur in the interior of the continent far from ($>10^3$ km) the active continental margin of the Paleo-Pacific subduction zone during the Early Cretaceous, responding to the intracontinental extension [14,15,110]. Additionally, recent seismological studies suggested that the back-arc extension of the Paleo-Pacific Ocean did not extend to the continental hinterland of the SGXR [111]. There is still a lack of robust evidence to demonstrate the far-field effect of the Paleo-Pacific plate on the intracontinental magmatism [16]. Therefore, the model involving the far-field effect of the Paleo-Pacific oceanic plate may not be responsible for the Zalute granitoid magmatism.

Here an alternative scenario that post-collisional extension related to the closure of Mongol–Okhotsk Ocean is favored based on the following observations. First, numerous studies have shown that post-collisional granitoid magmatism has a wide range in the compositions from high-K calc-alkaline (volume-dominated) to shoshonitic or alkaline granitoids [87,112]. The Zalute granitoids consist of the early Early Cretaceous intermediate-felsic intrusive suite (mostly high-K calc-alkaline in nature; Figure 6b) and middle Early Cretaceous alkaline intrusive suite, supporting the post-collisional magmatism. Secondly, the intermediate-felsic granitoids exhibit LREE enrichment relative to HREE (Figure 8a) and negative Nb-Ta anomalies (Figure 8b), commonly encountered in typical post-collisional

granitoids [113]. These observations are further supported by the discrimination diagram for tectonic setting that all the samples were plotted in the post-collisional granite field (Figure 6e).

The closure of the Mongol–Okhotsk Ocean occurred gradually from southwest to northeast by the scissor-type manner, terminating in the northeast in the Late Jurassic–early Early Cretaceous [11,25,107,114]. This interpretation is also supported by recent palaeomagnetic studies (e.g., [115]). The SGXR witnessed a transient Mongol–Okhotsk collisional orogeny in the latest Jurassic–earliest Cretaceous [16,39]. After early Early Cretaceous, the SGXR experienced intensive lithospheric extension, causing the Early Cretaceous giant granitoid-forming event, accompanied by widespread basin-and-range tectonism, metamorphic core complexes, rift basins, and large-scale magmatic-hydrothermal deposits [5,14,27].

The post-collisional granitoid magmatism could be generated by slab break-off or delamination of thickened crust, both of which can provide sufficient heat for crustal melting to produce resultant magmas [116,117]. The lack of S-type granite and crustal eclogite formed in thickened crust-related settings [114,118] implies that the Zalute granitoids seem not to be related to a thickened crust. Furthermore, the lithospheric delamination process generally produces a planar distribution pattern of granitoid rocks, whereas the slab break-off process can result in a narrow, linear distribution pattern of counterparts [117,119,120]. The Early Cretaceous granitoid magmatism in the SGXR is characterized by a NE-trending magmatic belt (Figure 1c) [9,16], implying break-off of the Mongol–Okhotsk oceanic slab.

Considering the above information, the parental magma of intermediate-felsic intrusive suite at Zalute may be interpreted tentatively to be formed dominantly by the partial melting of the underplated juvenile basaltic crust, followed by magmatic fractionation, which is associated with break-off of the Mongol–Okhotsk oceanic slab during the post-collisional extension (Figure 10).
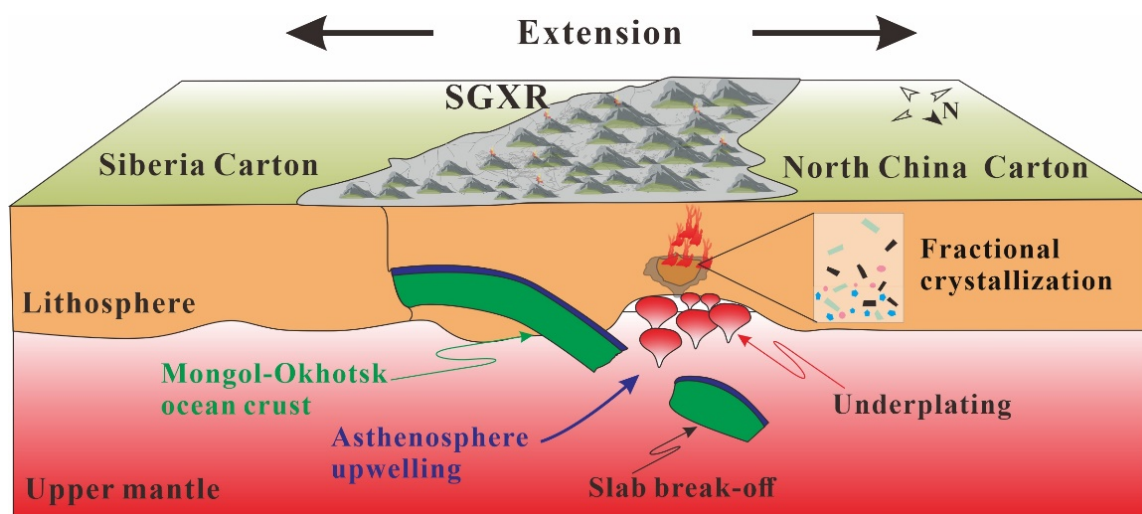

Figure 10. Schematic model for the early Early Cretaceous tectonic evolution of the SGXR.

6. Conclusions

1. SHRIMP zircon U–Pb dating for a suite of dioritic and granitic samples from Zalute gives a consistent crystallization age of ~137–136 Ma, involving quartz diorite dated at 136 ± 1.4 Ma, monzogranite at 136 ± 0.8 Ma, and granite porphyry at 137 ± 1.3 Ma. The new geochronological data reveals that the Zalute intermediate-felsic granitoids were formed in the early Early Cretaceous.

2. The quartz diorite, monzogranite, and granite porphyry, constituting an I-type intrusive suite, are characterized by uniform and depleted Sr–Nd–Hf isotopic compositions (initial $^{87}Sr/^{86}Sr$ ratios of 0.7035 to 0.7049, $\varepsilon_{Nd}(t)$ of −0.02 to 2.6, and $\varepsilon_{Hf}(t)$ of +6.8 to +9.6), indicating that they share a common origin. Their parental magma was dominantly derived from the partial melting of underplated mafic lower crust with minor ancient crustal components. Combined with their close spatial–temporal distribution pattern, common source, and compositional trend, a magmatic fractionation model of

the Zalute intermediate-felsic intrusive suite is proposed, with a close petrogenetic relation between quartz diorites, monzogranites, and granite porphyries.

3. The post-collisional extension related to the closure of the Mongol–Okhotsk Ocean and subsequent slab break-off played an important role in the generation of the Zalute intermediate-felsic intrusive suite.

References

1. Dong, Y.; Ge, W.C.; Yang, H.; Zhao, G.; Wang, Q.; Zhang, Y.; Su, L. Geochronology and geochemistry of Early Cretaceous volcanic rocks from the Baiyingaolao Formation in the central Great Xing'an Range, NE China, and its tectonic implications. *Lithos* **2014**, *205*, 168–184. [CrossRef]

2. Niu, Y.; Zhao, Z.; Zhu, D.-C.; Mo, X. Continental collision zones are primary sites for net continental crust growth: A testable hypothesis. *Earth-Sci. Rev.* **2013**, *127*, 96–110. [CrossRef]

3. Li, X.-H.; Li, Z.-X.; Li, W.-X.; Wang, X.-C.; Gao, Y. Revisiting the "C-type adakites" of the Lower Yangtze River Belt, central eastern China: In-situ zircon Hf–O isotope and geochemical constraints. *Chem. Geol.* **2013**, *345*, 1–15. [CrossRef]

4. Jahn, B.-M.; Litvinovsky, B.; Zanvilevich, A.; Reichow, M. Peralkaline granitoid magmatism in the Mongolian–Transbaikalian Belt: Evolution, petrogenesis and tectonic significance. *Lithos* **2009**, *113*, 521–539. [CrossRef]

5. Wu, F. Highly fractionated I-type granites in NE China (I): Geochronology and petrogenesis. *Lithos* **2003**, *66*, 241–273. [CrossRef]

6. Jiang, S.Y.; Zhao, K.D.; Jiang, H.; Su, H.M.; Xiong, S.Y.; Xiong, Y.Q.; Xu, Y.M.; Zhang, W.; Zhu, Y.L. Spatiotemporal distribution, geological characteristics and metallogenic mechanism of tungsten and tin deposits in China: An overview. *ChinSciBull* **2020**, *65*, 1–16. (In Chinese with English abstract)

7. Zheng, Y.-F.; Xu, Z.; Chen, L.; Dai, L.-Q.; Zhao, Z.-F. Chemical geodynamics of mafic magmatism above subduction zones. *J. Asian Earth Sci.* **2020**, *194*, 104185. [CrossRef]

8. Mao, J.W.; Xie, G.Q.; Yuan, S.D.; Liu, P.; Meng, X.Y.; Zhou, Z.H.; Zheng, W. Current research progress and future trends of porphyry–skarn copper and granite-related tin polymetallic deposits in the Circum Pacific metallogenic belts. *Acta Petrol. Sin.* **2018**, *34*, 2501–2517. (In Chinese with English abstract)

9. Li, S.; Chung, S.-L.; Wang, T.; Wilde, S.A.; Chu, M.-F.; Pang, C.-J.; Guo, Q.-Q. Water-fluxed crustal melting and petrogenesis of large-scale Early Cretaceous intracontinental granitoids in the southern Great Xing'an Range, North China. *GSA Bull.* **2017**, *130*, 580–597. [CrossRef]

10. Wang, Q.; Hawkesworth, C.J.; Wyman, D.; Chung, S.-L.; Wu, F.-Y.; Li, X.-H.; Li, Z.-X.; Gou, G.-N.; Zhang, X.-Z.; Tang, G.-J.; et al. Pliocene-Quaternary crustal melting in central and northern Tibet and insights into crustal flow. *Nat. Commun.* **2016**, *7*, 11888. [CrossRef]

11. Xu, W.; Sun, C.; Tang, J.; Luan, J.; Wang, F. Basement nature and tectonic evolution of the Xing'an–Mongolian Orogenic Belt. *Earth Sci.* **2019**, *44*, 1620–1646. (In Chinese with English abstract)

12. Wilkinson, J.J. Triggers for the formation of porphyry ore deposits in magmatic arcs. *Nat. Geosci.* **2013**, *6*, 917–925. [CrossRef]

13. Wei, W.; Zou, T.; Huang, X.; Jiang, B.; Zhu, X.; Wu, X. Petrogenesis of early Cretaceous granitoids in the southern Great Xing'an Range, NE China: Constraints from the Haliheiba pluton. *Geo-Chem* **2020**, *80*. [CrossRef]

14. Ouyang, H.; Mao, J.; Zhou, Z.; Su, H. Late Mesozoic metallogeny and intracontinental magmatism, southern Great Xing'an Range, northeastern China. *Gondwana Res.* **2015**, *27*, 1153–1172. [CrossRef]

15. Wang, T.; Guo, L.; Zhang, L.; Yang, Q.; Zhang, J.; Tong, Y.; Ye, K. Timing and evolution of Jurassic–Cretaceous granitoid magmatisms in the Mongol–Okhotsk belt and adjacent areas, NE Asia: Implications for transition from contractional crustal thickening to extensional thinning and geodynamic settings. *J. Asian Earth Sci.* **2015**, *97*, 365–392. [CrossRef]

16. Li, S.; Chung, S.-L.; Wang, T.; Wilde, S.A.; Chu, M.-F.; Guo, Q.-Q. Tectonic significance and geodynamic processes of large-scale Early Cretaceous granitoid magmatic events in the southern Great Xing'an Range, North China. *Tectonics* **2017**, *36*, 615–633. [CrossRef]

17. Guo, X.-G.; Li, J.-W.; Zhang, D.-H.; Xue, F.; Xian, H.-B.; Wang, S.-J.; Jiao, T.-L. Petrogenesis and tectonic setting of igneous rocks from the Dongbulage porphyry Mo deposit, Great Hinggan Range, NE China: Constraints from geology, geochronology, and isotope geochemistry. *Ore Geol. Rev.* **2020**, *120*, 103326. [CrossRef]

18. Wan, L.; Lu, C.; Zeng, Z.; Mohammed, A.S.; Liu, Z.; Dai, Q.; Chen, K. Nature and significance of the late Mesozoic granitoids in the southern Great Xing'an range, eastern Central Asian Orogenic Belt. *Int. Geol. Rev.* **2018**, *61*, 584–606. [CrossRef]

19. Yang, F.; Sun, J.-G.; Wang, Y.; Fu, J.; Na, F.; Fan, Z.; Hu, Z. Geology, Geochronology and Geochemistry of Weilasituo Sn-Polymetallic Deposit in Inner Mongolia, China. *Minerals* **2019**, *9*, 104. [CrossRef]

20. Zhang, K.-J. Genesis of the Late Mesozoic Great Xing'an Range Large Igneous Province in eastern central Asia: A Mongol–Okhotsk slab window model. *Int. Geol. Rev.* **2014**, *56*, 1557–1583. [CrossRef]

21. Wang, X.; Xu, D.; Lv, X.; Wei, W.; Mei, W.; Fan, X.; Sun, B. Origin of the Haobugao skarn Fe-Zn polymetallic deposit, Southern Great xing'an range, NE China: Geochronological, geochemical, and Sr-Nd-Pb isotopic constraints. *Ore Geol. Rev.* **2018**, *94*, 58–72. [CrossRef]

22. Ma, X.H.; Chen, B. The source of hydrothermal fluids and mineralization in the Aolunhua porphyry Mo-Cu deposit, southern Da Hinggan Mountains: Constraints from stable (C, H, O, and S) and radiogenic (Pb) isotopes. *J. Jilin Univ.* **2011**, *41*, 1770–1783. (In Chinese with English abstract)

23. Liu, J.; Qin, M.; Cai, Y.; Liu, Z.; Zhang, Z.; Yao, L. Late Mesozoic tectonic evolution of the southern Great Xing'an Range, northeastern China: Constraints from detrital zircon U–Pb and Hf isotopes of Late Cretaceous sandstones in the southwestern Songliao Basin. *Geol. J.* **2019**, *55*, 4415–4425. [CrossRef]

24. Ying, J.-F.; Zhou, X.-H.; Zhang, L.-C.; Wang, F. Geochronological framework of Mesozoic volcanic rocks in the Great Xing'an Range, NE China, and their geodynamic implications. *J. Asian Earth Sci.* **2010**, *39*, 786–793. [CrossRef]

25. Ji, Z.; Ge, W.-C.; Wang, Q.-H.; Yang, H.; Zhao, G.-C.; Bi, J.-H.; Dong, Y. Petrogenesis of Early Cretaceous volcanic rocks of the Manketouebo Formation in the Wuchagou region, central Great Xing'an Range, NE China, and tectonic implications: Geochronological, geochemical, and Hf isotopic evidence. *Int. Geol. Rev.* **2015**, *58*, 556–573. [CrossRef]

26. Zhang, J.-H.; Ge, W.-C.; Wu, F.; Wilde, S.A.; Yang, J.-H.; Liu, X.-M. Large-scale Early Cretaceous volcanic events in the northern Great Xing'an Range, Northeastern China. *Lithos* **2008**, *102*, 138–157. [CrossRef]

27. Zhang, C.; Quan, J.-Y.; Zhang, Y.-J.; Liu, Z.-H.; Li, W.; Wang, Y.; Qian, C.; Zhang, L.; Ge, J.-T. Late Mesozoic tectonic evolution of the southern Great Xing'an Range, NE China: Evidence from whole-rock geochemistry, and zircon U Pb ages and Hf isotopes from volcanic rocks. *Lithos* **2020**, 105409. [CrossRef]

28. Shen, P.; Shen, Y.; Pan, H.; Wang, J.; Zhang, R.; Zhang, Y. Baogutu Porphyry Cu-Mo-Au Deposit, West Junggar, Northwest China: Petrology, Alteration, and Mineralization. *Econ. Geol.* **2010**, *105*, 947–970. [CrossRef]

29. Mi, K.F.; Yan, T.J.; Lü, Z.C. Zircon U–Pb Geochronology of Baiyingaolao Formation from the Hadayingzi Region in the southern Great Xing'an Range, Northeast China. *Geol. Soc. China* **2019**, *93*, 39–40.

30. Mi, K.-F.; Lü, Z.; Yan, T.-J.; Zhao, S.-J.; Yu, H.-Y. SHRIMP U-Pb zircon geochronology and Hf isotope analyses of Middle Permian–early triassic intrusions in southern Manzhouli area, Northeast China: Implications for the subduction of Mongol-Okhotsk plate beneath the Erguna massif. *Int. Geol. Rev.* **2019**, *62*, 549–567. [CrossRef]

31. Zhang, C.; Quan, J.; Liu, Z.; Xu, Z.; Pang, X.; Zhang, Y. Geochemical Characteristics and Geological Significance of Meta-Volcanic Rocks of the Bainaimiao Group, Sonid Right Banner, Inner Mongolia, China. *J. Earth Sci.* **2019**, *30*, 272–285. [CrossRef]

32. Chen, A.; Zhou, D.; Zhang, Q.; Yang, Z. Age, Geochemistry, and Tectonic Implications of Dulaerqiao Granite, Inner Mongolia. *J. Earth Sci.* **2018**, *29*, 78–92. [CrossRef]

33. Zhao, X.; Zhou, W.; Fu, D.; Huang, B.; Ge, M. Isotope Chronology and Geochemistry of the Lower Carboniferous Granite in Xilinhot, Inner Mongolia, China. *J. Earth Sci.* **2018**, *29*, 280–294. [CrossRef]

34. Şengör, A.; Natal'In, B.; Burtman, V. Evolution of the Altaid tectonic collage and Palaeozoic crustal growth in Eurasia. *Nature* **1993**, *364*, 299–307. [CrossRef]

35. Gong, M.; Tian, W.; Fu, B.; Wang, S.; Dong, J. Zircon Hf-O isotopic constraints on the origin of Late Mesozoic felsic volcanic rocks from the Great Xing'an Range, NE China. *Lithos* **2018**, *308*, 412–427. [CrossRef]

36. Xiao, W.; Windley, B.F.; Hao, J.; Zhai, M. Accretion leading to collision and the Permian Solonker suture, Inner Mongolia, China: Termination of the central Asian orogenic belt. *Tectonics* **2003**, *22*, 22. [CrossRef]

37. Zhang, J.-H.; Gao, S.; Ge, W.-C.; Wu, F.-Y.; Yang, J.-H.; Wilde, S.A.; Li, M. Geochronology of the Mesozoic volcanic rocks in the Great Xing'an Range, northeastern China: Implications for subduction-induced delamination. *Chem. Geol.* **2010**, *276*, 144–165. [CrossRef]

38. Tomurtogoo, O.; Windley, B.; Kröner, A.; Badarch, G.; Liu, D. Zircon age and occurrence of the Adaatsag ophiolite and Muron shear zone, central Mongolia: Constraints on the evolution of the Mongol–Okhotsk ocean, suture and orogen. *J. Geol. Soc.* **2005**, *162*, 125–134. [CrossRef]

39. Yang, Y.-T.; Guo, Z.-X.; Song, C.-C.; Li, X.-B.; He, S. A short-lived but significant Mongol–Okhotsk collisional orogeny in latest Jurassic–earliest Cretaceous. *Gondwana Res.* **2015**, *28*, 1096–1116. [CrossRef]

40. Li, Y.; Xu, W.; Zhu, R.-X.; Wang, F.; Ge, W.-C.; Sorokin, A. Late Jurassic to early Early Cretaceous tectonic nature on the NE Asian continental margin: Constraints from Mesozoic accretionary complexes. *Earth-Science Rev.* **2020**, *200*, 103042. [CrossRef]

41. Guo, F.; Fan, W.; Li, C.; Gao, X.; Miao, L. Early Cretaceous highly positive ε Nd felsic volcanic rocks from the Hinggan Mountains, NE China: Origin and implications for Phanerozoic crustal growth. *Acta Diabetol.* **2008**, *98*, 1395–1411. [CrossRef]

42. Zhou, J.-B.; Wilde, S.A. The crustal accretion history and tectonic evolution of the NE China segment of the Central Asian Orogenic Belt. *Gondwana Res.* **2013**, *23*, 1365–1377. [CrossRef]

43. Shi, G.; Liu, D.; Zhang, F.; Jian, P.; Miao, L.; Shi, Y.; Tao, H. SHRIMP U-Pb zircon geochronology and its implications on the Xilin Gol Complex, Inner Mongolia, China. *Chin. Sci. Bull.* **2003**, *48*, 2742–2748. [CrossRef]

44. Zhang, L.; Zhou, X.-H.; Ying, J.-F.; Wang, F.; Guo, F.; Wan, B.; Chen, Z.-G. Geochemistry and Sr–Nd–Pb–Hf isotopes of Early Cretaceous basalts from the Great Xinggan Range, NE China: Implications for their origin and mantle source characteristics. *Chem. Geol.* **2008**, *256*, 12–23. [CrossRef]

45. Guo, F.; Li, H.; Fan, W.; Li, J.; Zhao, L.; Huang, M.; Xu, W. Early Jurassic subduction of the Paleo-Pacific Ocean in NE China: Petrologic and geochemical evidence from the Tumen mafic intrusive complex. *Lithos* **2015**, *224*, 46–60. [CrossRef]

46. Dong, S.; Zhang, Y.; Zhang, F.; Cui, J.; Chen, X.; Zhang, S.-H.; Miao, L.; Li, J.; Shi, W.; Li, Z.; et al. Late Jurassic–Early Cretaceous continental convergence and intracontinental orogenesis in East Asia: A synthesis of the Yanshan Revolution. *J. Asian Earth Sci.* **2015**, *114*, 750–770. [CrossRef]

47. Guan, Q.-B.; Liu, Z.-H.; Wang, B.; Wang, X.; Wang, X.-A.; Shi, Q.; Chen, Y.-S. Middle Jurassic–Early Cretaceous tectonic evolution of the Bayanhushuo area, southern Great Xing'an Range, NE China: Constraints from zircon U–Pb geochronological and geochemical data of volcanic and subvolcanic rocks. *Int. Geol. Rev.* **2017**, *60*, 1883–1905. [CrossRef]

48. Williams, I.S. U-Th-Pb Geochronology by Ion Microprobe. *Appl. Microanal. Tech. Underst. Miner. Process.* **1997**, *7*, 1–35. [CrossRef]

49. Black, L.P.; Kamo, S.L.; Allen, C.M.; Aleinikoff, J.N.; Davis, D.W.; Korsch, R.J.; Foudoulis, C. TEMORA 1: A new zircon standard for Phanerozoic U–Pb geochronology. *Chem. Geol.* **2003**, *200*, 155–170. [CrossRef]

50. Song, B. Mount making and procedure of the SHRIMP dating. *Geol. Rev.* **2002**, *48*, 26–30. (In Chinese with English abstract)

51. Ludwig, K. ISOPLOT 3.00: A Geochronological Toolkit for Microsoft Excel (Berkeley Geochronology Center, Berkeley, California). *BGC Spec. Publ.* **2003**, *39*, 91–445.

52. Hu, Z.; Liu, Y.; Gao, S.; Liu, W.; Zhang, W.; Tong, X.; Lin, L.; Zong, K.; Li, M.; Chen, H.; et al. Improved in situ Hf isotope ratio analysis of zircon using newly designed X skimmer cone and jet sample cone in combination with the addition of nitrogen by laser ablation multiple collector ICP-MS. *J. Anal. At. Spectrom.* **2012**, *27*, 1391–1399. [CrossRef]

53. Lin, J.; Gao, S.; Hu, Z.; Gao, C.; Zong, K.; Wang, D. Continental and Oceanic Crust Recycling-induced Melt-Peridotite Interactions in the Trans-North China Orogen: U-Pb Dating, Hf Isotopes and Trace Elements in Zircons from Mantle Xenoliths. *J. Pet.* **2009**, *51*, 537–571. [CrossRef]

54. Wei, P.; Yu, X.; Li, D.; Liu, Q.; Yu, L.; Li, Z.; Geng, K.; Zhang, Y.; Sun, Y.; Chi, N. Geochemistry, Zircon U–Pb Geochronology, and Lu–Hf Isotopes of the Chishan Alkaline Complex, Western Shandong, China. *Minerals* **2019**, *9*, 293. [CrossRef]

55. Yang, Y.-H.; Wu, F.; Liu, Z.-C.; Chu, Z.-Y.; Xie, L.-W.; Yang, J.-H. Evaluation of Sr chemical purification technique for natural geological samples using common cation-exchange and Sr-specific extraction chromatographic resin prior to MC-ICP-MS or TIMS measurement. *J. Anal. At. Spectrom.* **2012**, *27*, 516. [CrossRef]

56. Li, C.-F.; Chen, F.; Li, X.-H. Precise isotopic measurements of sub-nanogram Nd of standard reference material by thermal ionization mass spectrometry using the NdO+ technique. *Int. J. Mass Spectrom.* **2007**, *266*, 34–41. [CrossRef]

57. Zhai, Q.-G.; Chung, S.-L.; Tang, Y.; Hu, P.-Y.; Jin, X.-C.; Wang, J.; Wang, H.-T.; Wang, K.-L.; Lee, H.-Y. Late Carboniferous ophiolites from the southern Lancangjiang belt, SW China: Implication for the arc–back-arc system in the eastern Paleo-Tethys. *Lithos* **2019**, *344*, 134–146. [CrossRef]

58. Liu, W.; Pan, X.; Xie, L.; Li, H. Sources of Material for the Linxi Granitoids, the Southern Segment of the Da Hinggan Mts.: When and How Continental Crust Grew? *Acta Petrol. Sin.* **2007**, *023*, 441–460. (In Chinese with English abstract)

59. Tang, G.; Wang, Q.; Wyman, D.A.; Li, Z.-X.; Zhao, Z.-H.; Jia, X.-H.; Jiang, Z.-Q. Ridge subduction and crustal growth in the Central Asian Orogenic Belt: Evidence from Late Carboniferous adakites and high-Mg diorites in the western Junggar region, northern Xinjiang (west China). *Chem. Geol.* **2010**, *277*, 281–300. [CrossRef]

60. Teng, C.; Zhang, X.; Zhou, Y.; Feng, J.; Li, S. LA–ICP–MS Zircon U–Pb Age and Geological Significance of the Early Cretaceous Monzogranite in Xiaowulangou, Xilinhot, Inner Mongolia. *Geoscience* **2019**, *33*, 1003–1014. (In Chinese with English abstract)

61. Middlemost, E.A. Naming materials in the magma/igneous rock system. *Earth-Sci. Rev.* **1994**, *37*, 215–224. [CrossRef]

62. Peccerillo, A.; Taylor, S.R. Geochemistry of eocene calc-alkaline volcanic rocks from the Kastamonu area, Northern Turkey. *Contrib. Miner. Pet.* **1976**, *58*, 63–81. [CrossRef]

63. Atherton, M. Slab breakoff: A model for Caledonian, Late Granite syn-collisional magmatism in the orthotectonic (metamorphic) zone of Scotland and Donegal, Ireland. *Lithos* **2002**, *62*, 65–85. [CrossRef]

64. Maniar, P.D.; Piccoli, P.M. Tectonic discrimination of granitoids. *GSA Bull.* **1989**, *101*, 635–643. [CrossRef]

65. Pearce, J.A.; Harris, N.B.W.; Tindle, A.G. Trace Element Discrimination Diagrams for the Tectonic Interpretation of Granitic Rocks. *J. Pet.* **1984**, *25*, 956–983. [CrossRef]

66. Allègre, C.; Minster, J. Quantitative models of trace element behavior in magmatic processes. *Earth Planet. Sci. Lett.* **1978**, *38*, 1–25. [CrossRef]

67. Sun, S.-S.; McDonough, W.F. Chemical and isotopic systematics of oceanic basalts: Implications for mantle composition and processes. *Geol. Soc. London Spéc. Publ.* **1989**, *42*, 313–345. [CrossRef]

68. Qiu, K.; Yu, H.; Wu, M.; Geng, J.; Ge, X.; Gou, Z.; Taylor, R.D. Discrete Zr and REE mineralization of the Baerzhe rare-metal deposit, China. *Am. Miner.* **2019**, *104*, 1487–1502. [CrossRef]

69. Qiu, Z.; Liang, D.; Wang, Y.; Sun, Y.; Li, L. Zircon REE, trace element characteristics and U–Pb chronology in the Baerzhe alkaline granite: Implications to the petrological genesis and mineralization. *Acta Petrol. Sin.* **2014**, *30*, 1757–1768. (In Chinese with English abstract)

70. Wang, Z.; Zhao, Y. Geochemistry and origin of the Baerzhe REE Nb–Be–Zr superlarge deposit. *Geochimica* **1997**, *26*, 24–35. (In Chinese with English abstract)

71. Yang, W.-B.; Niu, H.-C.; Shan, Q.; Sun, W.-D.; Zhang, H.; Li, N.-B.; Jiang, Y.-H.; Yu, X.-Y. Geochemistry of magmatic and hydrothermal zircon from the highly evolved Baerzhe alkaline granite: Implications for Zr–REE–Nb mineralization. *Miner. Depos.* **2013**, *49*, 451–470. [CrossRef]

72. Shen, L.; Zhao, S.; Yu, h.; Liu, Z.; Zhou, Y.; Su, J. Geochemical characteristics and zircon U–Pb ages of porphyroclastic lava in the Bayaerhushuo area, the south– central segment of Great Xing'an Range, and its geological significance. *Geol. Bull. China* **2019**, *38*, 1314–1326. (In Chinese with English abstract)

73. Yang, Q.; Guo, L.; Wang, T.; Zeng, T.; Zhang, L.; Tong, Y.; Shi, X.; Zhang, J. Geochronology, origin, sources and tectonic settings of Late Mesozoic two–stage granites in the Ganzhuermiao region, central and southern Da Hinggan Range, NE China. *Acta Petrol. Sin* **2014**, *30*, 1961–1981.

74. Yuan, J.G.; Gu, Y.C.; Xiao, R.; Qu, Y.Y.; Duan, K.B.; Han, Y. Geochemistry and Zircon U–Pb Dating of Granites in Early Cretaceous in Eastern Xilin Hot, Inner Mongolia and Its Geological Implications. *Geoscience* **2017**, *1*, 588–597. (In Chinese with English abstract)

75. Dong, X.; Niu, Y.; Zhang, Z.; Tian, Z.; He, Z. Mesozoic crustal evolution of southern Tibet: Constraints from the early Jurassic igneous rocks in the Central Lhasa terrane. *Lithos* **2020**, 105557. [CrossRef]

76. Ge, W.; Lin, Q.; Sun, D.; Wu, F.; Won, C.; Lee, M.; Jin, M.; Yun, S. Geochemical characteristics of the Mesozoic basalts in Da Hinggan Ling: Evidence of the mantle–crust interaction. *Acta Petrol. Sin.* **1999**, *15*, 396–407. (In Chinese with English abstract)

77. Mo, X.; Niu, Y.; Dong, G.; Zhao, Z.; Hou, Z.; Zhou, S.; Ke, S. Contribution of syncollisional felsic magmatism to continental crust growth: A case study of the Paleogene Linzizong volcanic Succession in southern Tibet. *Chem. Geol.* **2008**, *250*, 49–67. [CrossRef]

78. Chappell, B.W.; Bryant, C.J.; Wyborn, D. Peraluminous I-type granites. *Lithos* **2012**, *153*, 142–153. [CrossRef]

79. Martin, H.; Smithies, R.; Rapp, R.; Moyen, J.-F.; Champion, D. An overview of adakite, tonalite–trondhjemite–granodiorite (TTG), and sanukitoid: Relationships and some implications for crustal evolution. *Lithos* **2005**, *79*, 1–24. [CrossRef]

80. Yan, H.; Long, X.; Wang, X.-C.; Li, J.; Wang, Q.; Yuan, C.; Sun, M. Middle Jurassic MORB-type gabbro, high-Mg diorite, calc-alkaline diorite and granodiorite in the Ando area, central Tibet: Evidence for a slab roll-back of the Bangong-Nujiang Ocean. *Lithos* **2016**, *264*, 315–328. [CrossRef]

81. Smithies, R.H. The Archaean High-Mg Diorite Suite: Links to Tonalite-Trondhjemite-Granodiorite Magmatism and Implications for Early Archaean Crustal Growth. *J. Pet.* **2000**, *41*, 1653–1671. [CrossRef]

82. Xiao, Y.; Chen, S.; Niu, Y.; Wang, X.; Xue, Q.; Wang, G.; Gao, Y.; Gong, H.; Kong, J.; Shao, F.; et al. Mineral Compositions of Syn-collisional Granitoids and their Implications for the Formation of Juvenile Continental Crust and Adakitic Magmatism. *J. Pet.* **2020**. [CrossRef]

83. Zhang, Y.; Niu, Y.; Hu, Y.; Liu, J.; Ye, L.; Kong, J.; Duan, M. The syncollisional granitoid magmatism and continental crust growth in the West Kunlun Orogen, China—Evidence from geochronology and geochemistry of the Arkarz pluton. *Lithos* **2016**, *245*, 191–204. [CrossRef]

84. Chen, S.; Niu, Y.; Sun, W.; Zhang, Y.; Li, J.; Guo, P.; Sun, P. On the origin of mafic magmatic enclaves (MMEs) in syn-collisional granitoids: Evidence from the Baojishan pluton in the North Qilian Orogen, China. *Miner. Pet.* **2015**, *109*, 577–596. [CrossRef]

85. Huang, H.; Niu, Y.; Mo, X. Syn-collisional granitoids in the Qilian Block on the Northern Tibetan Plateau: A long-lasting magmatism since continental collision through slab steepening. *Lithos* **2016**, *246*, 99–109. [CrossRef]

86. Kong, J.; Niu, Y.; Duan, M.; Zhang, Y.; Hu, Y.; Li, J.; Chen, S. Petrogenesis of Luchuba and Wuchaba granitoids in western Qinling: Geochronological and geochemical evidence. *Miner. Pet.* **2017**, *111*, 887–908. [CrossRef]

87. Zhai, D.; Liu, Z.; Zhang, H.; Yao, M.; Wang, J.; Yang, Y. S–Pb isotopic geochemistry, U–Pb and Re–Os geochronology of the Huanggangliang Fe–Sn deposit, Inner Mongolia, NE China. *Ore Geol. Rev.* **2014**, *59*, 109–122. [CrossRef]

88. Hou, Z.; Zhang, H. Geodynamics and metallogeny of the eastern Tethyan metallogenic domain. *Ore Geol. Rev.* **2015**, *70*, 346–384. [CrossRef]

89. Green, T.H. Significance of Nb/Ta as an indicator of geochemical processes in the crust-mantle system. *Chem. Geol.* **1995**, *120*, 347–359. [CrossRef]

90. Hofmann, A.; Jochum, K.; Seufert, M.; White, W. Nb and Pb in oceanic basalts: New constraints on mantle evolution. *Earth Planet. Sci. Lett.* **1986**, *79*, 33–45. [CrossRef]

91. Ahmed, H.A.; Ma, C.-Q.; Wang, L.; Palinkaš, L.A.; Girei, M.B.; Zhu, Y.; Habib, M. Petrogenesis and Tectonic Implications of Peralkaline A-Type Granites and Syenites from the Suizhou-Zaoyang Region, Central China. *J. Earth Sci.* **2018**, *29*, 1181–1202. [CrossRef]

92. Qin, J.; Liu, C.; Chen, Y.; Deng, J. Timing of Lithospheric Extension in Northeastern China: Evidence from the Late Mesozoic Nianzishan A-Type Granitoid Complex. *J. Earth Sci.* **2019**, *30*, 689–706. [CrossRef]

93. Boehnke, P.; Watson, E.B.; Trail, D.; Harrison, T.M.; Schmitt, A.K. Zircon saturation re-revisited. *Chem. Geol.* **2013**, *351*, 324–334. [CrossRef]

94. King, P.; White, A.; Chappell, B.; Allen, C. Characterization and Origin of Aluminous A-type Granites from the Lachlan Fold Belt, Southeastern Australia. *J. Pet.* **1997**, *38*, 371–391. [CrossRef]

95. Su, H.-M.; Jiang, S.-Y.; Cao, M.-Y.; Luo, P. Rare-metal mineralization potential and petrogenesis of Early Cretaceous I-type granitic rocks in the Lizikeng volcanic basin of Jiangxi Province, South China: Evidence from mineralogy, geochemistry, and geochronology. *Miner. Deposita* **2019**, *55*, 453–468. [CrossRef]

96. Hu, F.; Hu, F.; Zhang, W.; Deng, Z.; Chen, X. A westward propagating slab tear model for Late Triassic Qinling Orogenic Belt geodynamic evolution: Insights from the petrogenesis of the Caoping and Shahewan intrusions, central China. *Lithos* **2016**, *262*, 486–506. [CrossRef]

97. Harrison, T.M.; Watson, E.B. The behavior of apatite during crustal anatexis: Equilibrium and kinetic considerations. *Geochim. Cosmochim. Acta* **1984**, *48*, 1467–1477. [CrossRef]

98. Wolf, M.B.; London, D. Apatite dissolution into peraluminous haplogranitic melts: An experimental study of solubilities and mechanisms. *Geochim. Cosmochim. Acta* **1994**, *58*, 4127–4145. [CrossRef]

99. Stepanov, A.; Mavrogenes, J.A.; Meffre, S.; Davidson, P. The key role of mica during igneous concentration of tantalum. *Contrib. Miner. Pet.* **2014**, *167*, 1–8. [CrossRef]

100. Bea, F.; Pereira, M.; Stroh, A. Mineral/leucosome trace-element partitioning in a peraluminous migmatite (a laser ablation-ICP-MS study). *Chem. Geol.* **1994**, *117*, 291–312. [CrossRef]

101. Ou, Q.; Wang, Q.; Wyman, D.A.; Zhang, H.-X.; Yang, J.-H.; Zeng, J.-P.; Hao, L.-L.; Chen, Y.-W.; Liang, H.; Qi, Y. Eocene adakitic porphyries in the central-northern Qiangtang Block, central Tibet: Partial melting of thickened lower crust and implications for initial surface uplifting of the plateau. *J. Geophys. Res. Solid Earth* **2017**, *122*, 1025–1053. [CrossRef]

102. Gao, Y.; Santosh, M.; Hou, Z.; Wei, R.; Ma, G.; Chen, Z.; Wu, J. High Sr/Y magmas generated through crystal fractionation: Evidence from Mesozoic volcanic rocks in the northern Taihang orogen, North China Craton. *Gondwana Res.* **2012**, *22*, 152–168. [CrossRef]

103. Sun, X.; Lu, Y.-J.; McCuaig, T.C.; Zheng, Y.-Y.; Chang, H.-F.; Guo, F.; Xu, L.-J. Miocene Ultrapotassic, High-Mg Dioritic, and Adakite-like Rocks from Zhunuo in Southern Tibet: Implications for Mantle Metasomatism and Porphyry Copper Mineralization in Collisional Orogens. *J. Pet.* **2018**, *59*, 341–386. [CrossRef]

104. Zhang, K.-J.; Yan, L.-L.; Ji, C. Switch of NE Asia from extension to contraction at the mid-Cretaceous: A tale of the Okhotsk oceanic plateau from initiation by the Perm Anomaly to extrusion in the Mongol–Okhotsk ocean? *Earth-Sci. Rev.* **2019**, *198*, 102941. [CrossRef]

105. Dash, B.; Yin, A.; Jiang, N.; Tseveendorj, B.; Han, B. Petrology, structural setting, timing, and geochemistry of Cretaceous volcanic rocks in eastern Mongolia: Constraints on their tectonic origin. *Gondwana Res.* **2015**, *27*, 281–299. [CrossRef]

106. Fan, W.-M.; Guo, F.; Wang, Y.-J.; Lin, G. Late Mesozoic calc-alkaline volcanism of post-orogenic extension in the northern Da Hinggan Mountains, northeastern China. *J. Volcanol. Geotherm. Res.* **2003**, *121*, 115–135. [CrossRef]

107. Cogné, J.-P.; Kravchinsky, V.A.; Halim, N.; Hankard, F. Late Jurassic-Early Cretaceous closure of the Mongol-Okhotsk Ocean demonstrated by new Mesozoic palaeomagnetic results from the Trans-Baïkal area (SE Siberia). *Geophys. J. Int.* **2005**, *163*, 813–832. [CrossRef]

108. Larson, R.L.; Olson, P. Mantle plumes control magnetic reversal frequency. *Earth Planet. Sci. Lett.* **1991**, *107*, 437–447. [CrossRef]

109. Breitsprecher, K.; Thorkelson, D.; Groome, W.; Dostal, J. Geochemical confirmation of the Kula-Farallon slab window beneath the Pacific Northwest in Eocene time. *Geology* **2003**, *31*, 351–354. [CrossRef]

110. Wang, F.; Zhou, X.-H.; Zhang, L.; Ying, J.-F.; Zhang, Y.-T.; Wu, F.; Zhu, R.-X. Late Mesozoic volcanism in the Great Xing'an Range (NE China): Timing and implications for the dynamic setting of NE Asia. *Earth Planet. Sci. Lett.* **2006**, *251*, 179–198. [CrossRef]

111. Zheng, T.; He, Y.; Yang, J.-H.; Zhao, L. Seismological constraints on the crustal structures generated by continental rejuvenation in northeastern China. *Sci. Rep.* **2015**, *5*, 14995. [CrossRef] [PubMed]

112. Liégeois, J.-P.; Navez, J.; Hertogen, J.; Black, R. Contrasting origin of post-collisional high-K calc-alkaline and shoshonitic versus alkaline and peralkaline granitoids. The use of sliding normalization. *Lithos* **1998**, *45*, 1–28. [CrossRef]

113. Goodenough, K.M.; Thomas, R.; De Waele, B.; Key, R.; Schofield, D.; Bauer, W.; Tucker, R.; Rafahatelo, J.-M.; Rabarimanana, M.; Ralison, A.; et al. Post-collisional magmatism in the central East African Orogen: The Maevarano Suite of north Madagascar. *Lithos* **2010**, *116*, 18–34. [CrossRef]

114. Zorin, Y. Geodynamics of the western part of the Mongolia–Okhotsk collisional belt, Trans-Baikal region (Russia) and Mongolia. *Tectonophysics* **1999**, *306*, 33–56. [CrossRef]

115. Ren, Q.; Zhang, S.; Wu, Y.; Yang, T.; Gao, Y.; Turbold, S.; Zhao, H.; Wu, H.; Li, H.; Fu, H.; et al. New Late Jurassic to Early Cretaceous Paleomagnetic Results From North China and Southern Mongolia and Their Implications for the Evolution of the Mongol-Okhotsk Suture. *J. Geophys. Res. Solid Earth* **2018**, *123*, 10–370. [CrossRef]

116. Bonin, B. Do coeval mafic and felsic magmas in post-collisional to within-plate regimes necessarily imply two contrasting, mantle and crustal, sources? A review. *Lithos* **2004**, *78*, 1–24. [CrossRef]

117. Luo, B.-J.; Zhang, H.; Xu, W.-C.; Guo, L.; Pan, F.-B.; Yang, H. The Middle Triassic Meiwu Batholith, West Qinling, Central China: Implications for the Evolution of Compositional Diversity in a Composite Batholith. *J. Pet.* **2015**, *56*, 1139–1172. [CrossRef]

118. Sheldrick, T.C.; Barry, T.L.; Van Hinsbergen, D.J.; Kempton, P.D. Constraining lithospheric removal and asthenospheric input to melts in Central Asia: A geochemical study of Triassic to Cretaceous magmatic rocks in the Gobi Altai (Mongolia). *Lithos* **2018**, 297–315. [CrossRef]

119. Rogers, R.D.; KárasonH; Van Der Hilst, R.D. Epeirogenic uplift above a detached slab in northern Central America. *Geology* **2002**, *30*, 1031–1034. [CrossRef]

120. Zhang, W.; Lentz, D.R.; Thorne, K.G.; Massawe, R.J. Late Silurian-Early Devonian slab break-off beneath the Canadian Appalachians: Insights from the Nashwaak Granite, west-central New Brunswick, Canada. *Lithos* **2020**, *358*, 105393. [CrossRef]